

ALIGN: Advanced Query Initialization with LiDAR–Image Guidance for Occlusion-Robust 3D Object Detection

Janghyun Baek¹, Mincheol Chang¹, Seokha Moon¹, Seung Joon Lee², Jinkyu Kim¹

¹CSE, Korea University ²CTO Division, LG Innotek

Abstract

Recent query-based 3D object detection methods using camera and LiDAR inputs have shown strong performance, but existing query initialization strategies—such as random sampling or BEV heatmap-based sampling—often result in inefficient query usage and reduced accuracy, particularly for occluded or crowded objects. To address this limitation, we propose **ALIGN** (Advanced query initialization with LiDAR and Image Guidance), a novel approach for occlusion-robust, object-aware query initialization. Our model consists of three key components: (i) Occlusion-aware Center Estimation (OCE), which integrates LiDAR geometry and image semantics to estimate object centers accurately; (ii) Adaptive Neighbor Sampling (ANS), which generates object candidates from LiDAR clustering and supplements each object by sampling spatially and semantically aligned points around it; and (iii) Dynamic Query Balancing (DQB), which adaptively balances queries between foreground and background regions. Our extensive experiments on the nuScenes benchmark demonstrate that ALIGN consistently improves performance across multiple state-of-the-art detectors, achieving gains of up to +0.9 mAP and +1.2 NDS, particularly in challenging scenes with occlusions or dense crowds. Our code will be publicly available upon publication.

Introduction

3D object detection is a fundamental capability in autonomous driving and robotics, as it directly influences an agent’s ability to perceive its environment, accurately identify obstacles, and navigate safely in complex urban environments. Combining multiple sensor modalities, particularly LiDAR and cameras, has recently emerged as the preferred strategy to enhance detection robustness and accuracy (Liang et al. 2018; Liu et al. 2022b; Drews et al. 2022; Zeng et al. 2022; Yang et al. 2022; Bai et al. 2022). While LiDAR provides accurate geometric information, cameras offer rich semantic and texture cues, enhancing performance under challenging conditions such as adverse lighting, heavy clutter, and occlusions.

Recently, query-based methods (Wang et al. 2023; Zhang et al. 2023; Gao et al. 2022; Zhao et al. 2024; Yao et al. 2021) have shown strong performance by training each learnable query to attend to potential objects in 3D space. Their effectiveness, however, depends on the query initialization strategy. As shown in Fig. 1(a) and (b), existing ap-

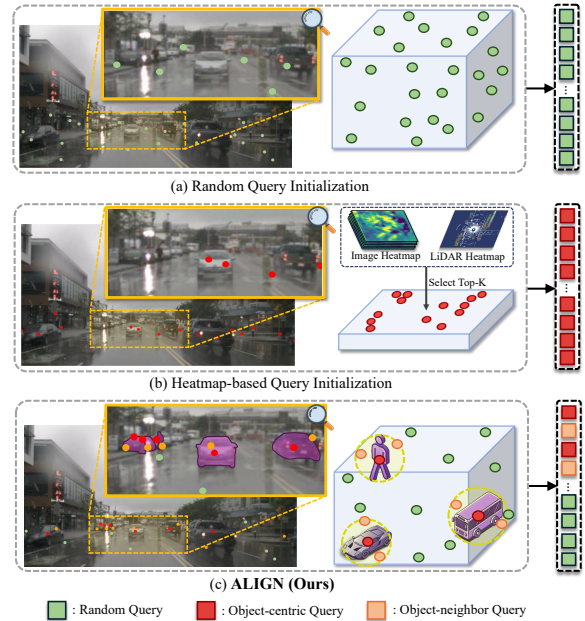


Figure 1: **Query Initialization Comparison.** Existing 3D object detectors typically adopt following query initialization schemes: (a) random initialization, where queries are sampled from uniformly distributed spatial regions, or (b) heatmap-based sampling from salient regions identified in BEV heatmaps. In contrast, (c) ALIGN accurately estimates object centers and samples queries in the vicinity of each center, while maintaining balanced background queries.

proaches primarily adopt the following strategies: (1) Random sampling (Yan et al. 2023b; Wang et al. 2022b; He and Todorovic 2022), which uniformly distributes queries regardless object relevance. While simple, this approach results in inefficient query usage, sparse coverage of key regions, and slower convergence; and (2) BEV heatmap-based sampling (Bai et al. 2022; Xie et al. 2023; Liu et al. 2022b; Liang et al. 2022), which allocates queries to salient regions inferred from (camera or LiDAR-based) BEV heatmaps. However, both strategies exhibit limitations in complex urban environments, often failing to capture occluded or small objects—common challenges in autonomous driving.

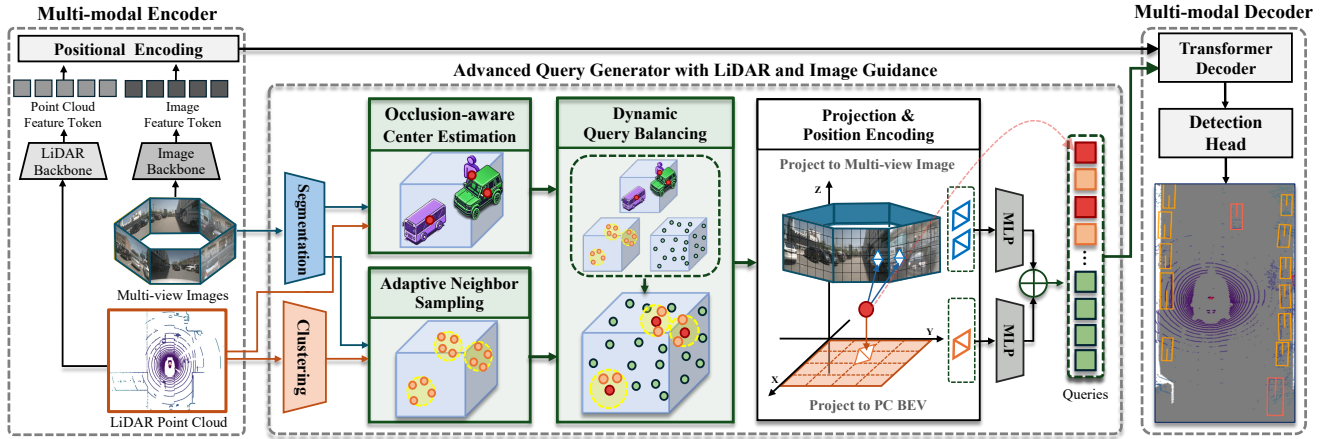


Figure 2: **An overview of our proposed method, ALIGN**, which enhances query-based 3D object detectors using a novel query initialization strategy. Our model consists of three main components: (i) Occlusion-aware Center Estimation (OCE) for accurate object center estimation from LiDAR point cloud and image segmentation, (ii) Adaptive Neighbor Sampling (ANS) for generating object candidates via LiDAR clustering and sampling object-aware queries around each object, and (iii) Dynamic Query Balancing (DQB) for augmenting background queries, ensuring a balanced foreground–background distribution.

To address these limitations, we introduce **ALIGN** (Advanced Query Initialization with LiDAR and Image Guidance), a novel object-aware query initialization strategy that samples queries from the vicinity of each estimated object center (see Fig 1(c)). We leverage both image semantics and LiDAR geometry to more accurately localize object centers. This approach is especially effective in detecting occluded, small, or distant objects—scenarios where conventional query initialization methods often struggle to perform effectively. Additionally, we find that augmenting background (i.e., non-object-aware) queries is also essential for improving overall detection performance, as it helps maintain a balanced distribution between foreground and background queries.

As shown in Fig 2, our object-aware query initialization method comprises three key components: (1) Occlusion-aware Center Estimation (OCE), which robustly estimates the 3D center positions of objects by leveraging LiDAR geometry and image semantics; (2) Adaptive Neighbor Sampling (ANS), which improves query coverage by sampling additional queries around LiDAR clusters, providing complementary spatial context for robust localization of partially occluded or densely clustered scenes; and (3) Dynamic Query Balancing (DQB), which adaptively adjusts the distribution between object-aware and background queries, mitigating overfitting to specific regions and ensuring robust detection performance across diverse scenarios.

To evaluate the effectiveness of our method, we conduct experiments on the widely used nuScenes (Caesar et al. 2020) benchmark, a large-scale autonomous driving dataset comprising multi-view camera and LiDAR. As our approach can be easily integrated into existing query-based 3D object detectors, we assess its effectiveness across several state-of-the-art models, including CMT (Yan et al. 2023b), TransFusion (Bai et al. 2022), SparseFusion (Xie et al. 2023), and FUTR3D (Chen et al. 2022a). Our extensive experiments

demonstrate that our query initialization strategy consistently and significantly improves the overall detection performance in terms of both mAP and NDS, with particularly strong gains in challenging scenarios involving occluded, small, distant, or densely packed objects. Our main contributions are summarized as follows:

- We propose a novel object-aware query initialization method for query-based 3D object detection, leveraging multi-modal sensor inputs from cameras and LiDAR.
- We introduce three key modules (occlusion-aware center estimation, adaptive neighbor sampling, and dynamic query balancing) to achieve effective object-aware query initialization.
- We apply our proposed query initialization method to various 3D query-based object detectors and observe consistent and substantial performance improvements on the nuScenes dataset.

Related Work

Query-based 3D Object Detection

Recently, query-based methods have shown strong performance in the 3D object detection by reformulating the task as a set prediction problem. A key factor in their effectiveness is the object query initialization strategy. Most existing approaches adopt one of the following two strategies: (i) random initialization and (ii) heatmap-based initialization.

Random Query Initialization. Most query-based 3D object detectors adopt random initialization following the DETR (Carion et al. 2020) paradigm. DETR3D (Wang et al. 2022a) samples 3D reference points and aggregates image features via projection. PETR (Liu et al. 2022a) introduces 3D position encoding into image features for implicit spatial grounding. FUTR3D (Chen et al. 2023a) fuses image and LiDAR features directly at each query via unified transformer

without BEV or explicit anchor priors. CMT (Yan et al. 2023b) improves modality alignment via coordinate-aware position embeddings. While simple and generalizable, random initialization suffers from suboptimal query placement and slower convergence.

Heatmap-based Query Initialization. To mitigate this issue, recent approaches adopt BEV heatmap-based initialization by sampling top- k salient regions. CenterFormer (Zhou et al. 2022) selects object centers from BEV heatmaps and uses their voxel features as queries. TransFusion (Bai et al. 2022) introduces an image-guided query by generating BEV heatmaps that fuse image semantics. SparseFusion (Xie et al. 2023) samples queries from both image and LiDAR heatmaps, jointly guided by geometry and semantics. EfficientQ3M (Van Geerenstein et al. 2024) combines BEV heatmaps with visual cues for query placement. FocalFormer3D (Chen et al. 2023a) employs a multi-stage heatmap encoder that accumulates salient regions for improved localization. Although these methods improve query efficiency by focusing on likely object regions, detecting small, occluded, or crowded objects remains challenging.

Thus, we propose an object-aware and scene-adaptive query initialization strategy that enhances 3D object detection in challenging scenes by aligning 3D LiDAR geometry with 2D image segmentation. To this end, we estimate object centers by combining segmentation-guided projection and LiDAR clustering, and adaptively sample segmentation-aligned neighbor anchors based on scene complexity. A fixed portion of background anchors is retained to ensure consistent spatial coverage. This adaptive strategy replaces confidence-based heuristics with spatially balanced and occlusion-robust initialization, unifying the strengths of object-centric and object-agnostic schemes.

Method

The overall framework of ALIGN is illustrated in Fig. 2. Given multi-view images and a LiDAR point cloud, ALIGN replaces heuristic query initialization with a structured generator that aligns geometric and semantic cues prior to transformer decoding. Specifically, the ALIGN produces three types of query anchors: object-centric anchors from OCE, which estimate 3D centers by projecting segmentation-aligned LiDAR points with class-specific depth offsets; neighbour anchors from ANS, which sample semantically consistent points around clustered regions to recover occluded or truncated objects; and background anchors from DQB, which dynamically balance query allocation based on scene density. All anchors are encoded in both camera and BEV spaces and passed as queries to the multi-modal transformer decoder, enabling improved spatial coverage and object localization. Because ALIGN is model-agnostic and initialization-only, it can be easily integrated into existing query-based 3D detectors without modifying their detection heads or training objectives.

Occlusion-Aware Center Estimation

Prior methods (Bai et al. 2022; Yang et al. 2022; Xie et al. 2023) place queries on high-confidence peaks of LiDAR-

derived BEV heatmaps instead of estimating object centers explicitly. When returns are sparse, objects are occluded, or instances crowd together, these peaks drift or vanish, degrading localization. We therefore explicitly infer centers by fusing LiDAR geometry with image segmentation, introducing an Occlusion-Aware Center Estimation (OCE) module that remains reliable under occlusion and density (Fig. 3(a)).

3D LiDAR points (x, y, z) are projected onto the surrounding image planes, yielding image coordinates (u, v) via known calibration parameters. Let $\mathcal{M}_{i,j}$ denote the segmentation mask of the j -th object in the i -th camera view. We retain only the points whose projections satisfy $(u, v) \in \mathcal{M}_{i,j}$ and define $\mathbf{P}_{i,j}$:

$$\mathbf{P}_{i,j} = \{(u, v, x, y, z) \mid (u, v) \in \mathcal{M}_{i,j}\} \quad (1)$$

(u_c, v_c) denote the center of the 2D bounding box of $\mathcal{M}_{i,j}$. We select four LiDAR points closest to (u_c, v_c) in image space,

$$\mathcal{S}_{i,j} = \{\text{Top}_4(\mathbf{P}_{i,j}, \|(u, v) - (u_c, v_c)\|_2)\} \quad (2)$$

and estimate a local homography $\mathbf{H}_{i,j}$ that maps image to LiDAR coordinates,

$$[x, y, z]^\top = \mathbf{H}_{i,j}[u, v, 1]^\top. \quad (3)$$

Applying $\mathbf{H}_{i,j}$ to the 2D center (u_c, v_c) yields an object’s coarse 3D surface point

$$\mathbf{p}_{\text{surf}} = \mathbf{H}_{i,j}[u_c, v_c, 1]^\top. \quad (4)$$

Although \mathbf{p}_{surf} lies on the visible surface of the object, it does not coincide with the true geometric center due to its inherent surface bias. To address this, we apply a class-specific *depth compensation offset* d , which approximates the displacement between the visible surface and the geometric center along the depth axis. This offset is applied along the LiDAR ray direction, represented by the unit vector from the origin to \mathbf{p}_{surf} , resulting in the final estimated center set:

$$\mathbf{P}_{\text{OCE}} = \left\{ \mathbf{p}_{\text{surf}} + d \cdot \frac{\mathbf{p}_{\text{surf}}}{\|\mathbf{p}_{\text{surf}}\|_2} \right\}. \quad (5)$$

Adaptive Neighbor Sampling

OCE provides reasonable center estimates even under partial occlusion, but it inherently depends on segmentation quality. In particular, when large or close-range objects are only partially within a camera’s field of view, the resulting masks are incomplete, hindering accurate center estimation.

To address this, we introduce the Adaptive Neighbor Sampling (ANS) module (Fig. 3(b)). We apply DBSCAN (Schubert et al. 2017) to the LiDAR point cloud to identify clusters corresponding to potential objects. The core points of each cluster form $\mathbf{p}_{\text{cluster}}$ and serve as initial query anchors. Inspired by Deformable DETR (Zhu et al. 2021), which samples keypoints around query anchors, we sample additional points around each core to capture the spatial extent of objects. For each cluster core point in $\mathbf{p}_{\text{cluster}}$, we randomly sample N neighbors points within a sampling range r :

$$\mathbf{P}_{\text{nbr}} = \left\{ \mathbf{p}_i \mid \text{dist}(\mathbf{p}_i, \mathbf{p}_{\text{cluster}}) < r, i = 1, \dots, N \right\}. \quad (6)$$

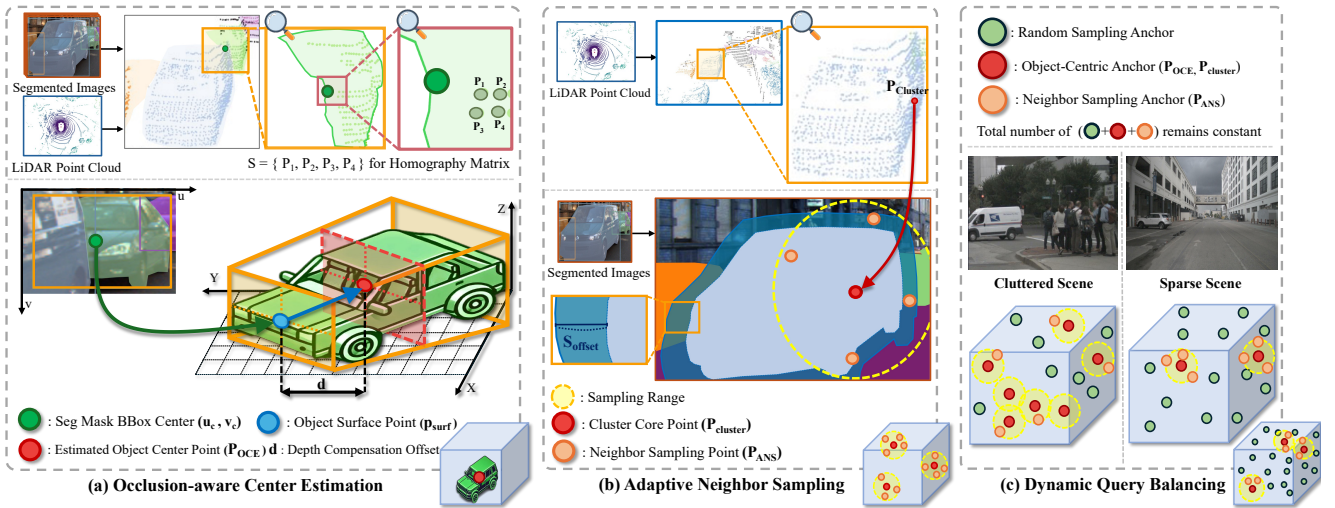


Figure 3: **Detailed illustration of each module.** (a) OCE predicts object centers by integrating LiDAR geometry and image semantics, improving localization under occlusions. (b) ANS samples segmentation-aligned neighbors around each LiDAR cluster core for expands anchor coverage and feature diversity. (c) DQB balances object-centric and background queries by scene complexity, retaining fixed portion of background anchors for spatial coverage. These modules jointly optimize query initialization, leading to robust 3D object detection.

This naïve sampling may select irrelevant regions such as walls or the ground particularly in cluttered scenes. To suppress such noise, we retain only the neighbor points whose projections lie within a semantic offset S_{offset} from the segmentation mask \mathcal{M}_i , forming the sampling set \mathbf{P}_{ANS} :

$$\mathbf{P}_{\text{ANS}} = \left\{ \mathbf{p}_i \in \mathbf{P}_{\text{nbr}} \mid \text{dist}(\Pi(\mathbf{p}_i), \mathcal{M}_i) < S_{\text{offset}} \right\}. \quad (7)$$

If the number of retained points in \mathbf{P}_{ANS} is insufficient, the sampling and filtering steps are repeated up to three times to ensure adequate coverage. By uniting geometry-based clustering with semantic filtering, ANS complements OCE for occlusion-robust query initialization, yielding the core anchors set $\mathbf{p}_{\text{cluster}}$ and the refined neighbor set \mathbf{P}_{ANS} .

Dynamic Query Balancing

A fixed query budget must capture both fine-grained object details and broad background context. Allocating the surplus entirely to random anchors under-explores sparse scenes, while using only object-centric anchors wastes capacity in crowded scenes. As shown in Fig. 3(c), DQB addresses this by balancing the number of queries between ANS neighbor queries and randomly sampled background anchors. After assigning object-centric anchors (N_{OCE} from OCE and N_{cluster} from LiDAR clustering), the remaining budget is partitioned as follows:

$$N_{\text{ANS}} = \nabla_{\text{bal}}(N_{\text{total}} - N_{\text{OCE}} - N_{\text{cluster}}), \quad (8)$$

$$N_{\text{rand}} = (1 - \nabla_{\text{bal}})(N_{\text{total}} - N_{\text{OCE}} - N_{\text{cluster}}), \quad (9)$$

where N_{total} is the overall query budget and $\nabla_{\text{bal}} \in [0, 1]$ is a fixed hyperparameter that balances object-centric refinement and background exploration. The remaining budget is divided into N_{ANS} neighbor queries and N_{rand} background queries. The neighbor queries are allocated evenly

across object candidates—resulting in fewer samples per object in crowded scenes—to maintain background coverage, and denser sampling in sparse scenes to improve localization. This adaptive allocation strategy enables robust query placement across diverse scene complexities and contributes to the performance improvements reported in Tables 6.

Loss Functions. We employ a simple loss function consisting of classification and 3D bounding box regression. Set prediction is performed via bipartite matching using the Hungarian algorithm (Kuhn 1955). Focal loss (Lin et al. 2017) L_{cls} is applied for classification and L1 loss for bounding box regression (L_{reg}). The final loss is a weighted sum of these components, as shown in Eq. 10. In all experiments, we set $\lambda_1 = 2.0$ and $\lambda_2 = 0.25$.

$$L_{\text{total}} = \lambda_1 L_{\text{cls}}(\mathbf{c}, \hat{\mathbf{c}}) + \lambda_2 L_{\text{reg}}(\mathbf{b}, \hat{\mathbf{b}}), \quad (10)$$

Experiments

Dataset and Metrics. We use nuScenes dataset (Caesar et al. 2020) to evaluate our method’s effectiveness, which provides six cameras, five radars, and one LiDAR sensor, yielding a 360° field of view. The dataset contains 1,000 scenes split into 700/150/150 for training/validation/test and includes $\sim 1.4\text{M}$ annotated 3D boxes over 10 classes. We report mean Average Precision (mAP) and nuScenes Detection Score (NDS) as the main metrics.

Implementation Details. To demonstrate the effectiveness of our method, we implement ALIGN on four query-based LiDAR-camera detectors: CMT (Yan et al. 2023b), TransFusion (Bai et al. 2022), FUTR3D (Chen et al. 2023a), and SparseFusion (Xie et al. 2023), using MMDetection3D (Contributors 2020). For fair comparison, we retain each baseline’s backbone, ResNet-50 (He et al. 2015)

Method	Query Init.			Validation		Test	
	Random	Heatmap	ALIGN	mAP \uparrow	NDS \uparrow	mAP \uparrow	NDS \uparrow
UVTR (Li et al. 2022)	✓			63.9	69.7	65.4	70.4
Transfusion (Bai et al. 2022)		✓		67.3	70.9	68.9	71.6
CMT-small (Yan et al. 2023a)	✓			67.4	70.2	68.8	71.6
FUTR3D (Chen et al. 2023a)	✓			67.4	70.9	69.4	72.1
ObjectFusion (Cai et al. 2023)		✓		69.8	72.3	71.0	73.3
EfficientQ3M (Van Geerenstein et al. 2024)		✓		70.5	72.6	71.2	73.5
SparseFusion (Xie et al. 2023)		✓		70.5	72.8	72.0	73.8
FocalFormer3D (Chen et al. 2023b)		✓		70.5	73.1	71.6	73.9
CMT-Large (Yan et al. 2023a)	✓			70.3	72.9	72.0	74.1
Transfusion + ALIGN			✓	67.7 (+0.4)	71.3 (+0.4)	–	–
CMT-small + ALIGN			✓	68.3 (+0.9)	71.4 (+1.2)	69.3 (+0.5)	72.2 (+0.6)
FUTR3D + ALIGN			✓	68.2 (+0.8)	71.8 (+0.9)	–	–
SparseFusion + ALIGN			✓	70.9 (+0.4)	73.1 (+0.3)	–	–
CMT-Large + ALIGN			✓	71.1 (+0.8)	73.3 (+0.4)	72.4 (+0.4)	74.5 (+0.4)

Table 1: **Performance comparison on nuScenes dataset.** We evaluate various query-based 3D object detectors under different query initialization strategies. Replacing the original initialization with ALIGN consistently improves mAP and NDS across all baselines. The best results are highlighted in **bold**. All results are reported without test-time augmentation.

or VOVNet (Lee et al. 2019) for image and VoxelNet (Yan, Mao, and Li 2018) for LiDAR. Segmentation masks are produced by Mask R-CNN (He et al. 2017), pretrained on nuImages (Caesar et al. 2020), with FP16 inference at 800×320 resolution. Region of interest (RoI) is defined as $[-54, 54]m$ in X/Y and $[-5, 3]m$ in Z . All feature and query embeddings use dimension $D = 256$. We follow each baseline’s hyperparameters to ensure a fair comparison.

Training Strategy. We train our model on 4 GPUs for 20 epochs with batch size 8, using the nuScenes dataset for training and evaluation. We use RTX3090 for models with ResNet-50 (He et al. 2015) and A6000 Ada for those with VOVNet (Lee et al. 2019). To balance class distribution, we incorporated CBGS (Zhu et al. 2019) and AutoAlign (Chen et al. 2022b). We adopt the AdamW optimizer (Loshchilov and Hutter 2019) with a learning rate of 9×10^{-5} , following a cyclic learning rate policy (Smith 2017), and set the weight decay to 1×10^{-2} . We do not apply any test-time augmentation in the reported results.

Experimental Results

Quantitative Results. Table 1 compares five query-based detectors with publicly available training code and configurations (TransFusion (Bai et al. 2022), CMT-small (Yan et al. 2023a), FUTR3D (Chen et al. 2023a), SparseFusion (Xie et al. 2023), and CMT-Large (Yan et al. 2023a)) on the nuScenes validation and test sets, before and after applying ALIGN. ALIGN consistently improves both mAP and NDS across all baselines, with particularly large gains observed in models that use uniform query initialization. For example, CMT-small improves from 70.3 to 71.1 mAP (+0.8) and from 72.9 to 73.3 NDS (+0.4), while FUTR3D gains +0.8 mAP and +0.9 NDS. In contrast, heatmap-guided mod-

els such as TransFusion and SparseFusion show smaller yet consistent improvements (+0.4 mAP / +0.3 NDS), suggesting that ALIGN is most beneficial when no object-specific prior is used in initialization. CMT-Large achieves the highest overall performance (71.1 mAP / 73.3 NDS), confirming that ALIGN scales well to stronger architectures.

These results demonstrate that replacing original query initialization with semantically grounded, geometry-aware anchors enables precise attention allocation and robust performance gains across architectures.

Analysis across Occlusion Levels. The nuScenes benchmark (Caesar et al. 2020) defines occlusion levels from 1 (heavily occluded) to 4 (fully visible). We analyze detection performance across these levels to evaluate ALIGN’s robustness under occlusion. As shown in Table 2, ALIGN consistently improves mAP across all visibility levels and object categories. Notably, the performance gains peak under heavy occlusion (Occ. 1), with a +1.4 mAP increase over the baseline, compared to only +0.7 at Occ. 4. This confirms that ALIGN is particularly effective under heavy occlusion, where standard query initialization often fails. Furthermore, improvements are especially large for small and thin objects such as *Bicycle* (+1.6) and *Traffic Cone* (+2.2), indicating that ALIGN’s segmentation-aligned and geometry-aware anchors better capture challenging instances that are easily missed by conventional approaches.

Ablation of ALIGN Modules. Table 3 reports the ablation study on CMT-small using the nuScenes validation set. We progressively add Occlusion-aware Center Estimation (OCE), Adaptive Neighbor Sampling (ANS), and Dynamic Query Balancing (DQB) to isolate the effect of each module and assess their combined impact. Adding OCE improves performance from 67.4 / 70.2 to 68.0 / 70.8 (mAP / NDS),

Method	Occ.	mAP (%) \uparrow										
		Car	Truck	Bus	Tra.	Const.	Ped.	Moto.	Bike	Cone	Bar.	Total
CMT	1	49.7	8.40	15.5	17.6	4.30	56.8	41.7	19.0	20.5	25.6	25.9
CMT + ALIGN		51.1	9.97	18.3	17.8	4.75	57.6	44.1	21.3	22.4	25.8	27.3 (+1.4)
CMT	2	64.8	15.8	43.3	17.6	12.3	64.0	48.1	29.4	15.7	19.6	33.1
CMT + ALIGN		66.0	16.9	45.7	17.9	12.5	64.9	50.1	30.2	16.0	21.0	34.1 (+1.0)
CMT	3	79.3	40.4	65.5	31.2	25.2	71.0	73.5	48.5	29.2	44.2	50.8
CMT + ALIGN		79.9	40.9	66.3	32.0	25.3	71.7	74.7	50.1	30.3	45.5	51.8 (+1.0)
CMT	4	93.5	67.1	81.4	51.4	41.4	92.7	87.5	83.6	82.8	74.9	75.6
CMT + ALIGN		93.8	67.2	81.6	52.9	42.5	93.1	88.0	84.9	83.7	75.5	76.3 (+0.7)
CMT	Total	88.7	65.4	78.3	46.6	33.9	87.7	79.7	70.1	79.5	72.9	70.3
CMT + ALIGN		89.2	65.8	79.0	47.0	34.8	88.2	80.9	71.7	81.0	73.5	71.1 (+0.8)

Table 2: Detection performance across occlusion levels on the nuScenes validation set. **Occ.** denotes the occlusion level

	OCE	ANS	DQB	mAP \uparrow	NDS \uparrow
(a)				67.4	70.2
(b)	✓			68.0	70.8
(c)		✓		67.6	70.5
(d)	✓	✓		68.2	71.2
(e)	✓	✓	✓	68.3 (+0.9)	71.4 (+1.2)

Table 3: Ablation study of ALIGN modules

Depth Compensation Offset d	mAP \uparrow	NDS \uparrow
–	67.4	70.2
[0,0,0,0,0,0,0,0,0]	67.9	70.5
[1,2,2,2,2,0,0,0,0]	67.9	70.6
[1.5,3,3,3,3,0,0,0,0]	68.0	70.8

Table 4: Ablation of depth offsets in OCE.

confirming that segmentation-guided center estimation enhances query placement. Applying ANS alone yields 67.6 / 70.5, showing benefits from spatial sampling around LiDAR clusters even without explicit centers. Since DQB is not used in (c) and (d), samples per cluster is fixed. Combining OCE and ANS achieves 68.2 / 71.2, demonstrating complementary gains. Finally, incorporating DQB results in the highest performance (68.3 / 71.4), with a total improvement of +0.9 / +1.2 over the baseline. These results validate that each module contributes uniquely, and their integration yields consistent, additive gains in detection quality.

Depth Compensation Offset in OCE. Table 4 shows the effect of class-specific depth offsets d in OCE module. All offset-enabled variants outperform the baseline, confirming the value of explicit center estimation. Even with zero offset—using the visible surface as a proxy—performance improves, showing that coarse localization already helps. While mAP stays consistently strong, applying class-

Sampling Range	Sample Offset	mAP \uparrow	NDS \uparrow
–	–	67.4	70.2
0.015	15	67.5	70.3
0.015	30	67.6	70.5
0.030	15	67.5	70.4
0.030	30	67.6	70.5

Table 5: Ablation of sampling range and offset in ANS.

∇_{balance}	$N_{\text{ANS}}^{\text{max}}$	$N_{\text{rand}}^{\text{max}}$	mAP \uparrow	NDS \uparrow
0.32	288	612	65.1	69.3
0.16	144	756	68.1	71.2
0.08	72	828	68.3	71.4
0.04	54	846	68.2	71.2

Table 6: Ablation of balancing parameter in DQB.

specific offsets yields clear NDS gains by enhancing box size and orientation prediction. Offsets follow nuScenes class order (see supplementary material for detailed values).

Sampling Range and Offset in ANS. Table 5 shows the ablation results of sampling range and offset in the ANS module. The range is defined as a ratio of the Region of Interest, set to $[-54, 54]$ m (0.030 corresponds to 3.24 m). The offset denotes how many pixels beyond the segmentation mask are included. While range has limited impact, larger offsets consistently improve performance by expanding the mask region, allowing more valid points near object boundaries and enhancing query quality.

Balancing Parameter in DQB. Table 6 shows the effect of ∇_{balance} in DQB module. Performance peaks when ∇_{balance} is 0.08, and $N_{\text{ANS}}^{\text{max}}$ is 72. As the number of objects’ neighbor-sampled points increases (e.g., 288), the accuracy drops significantly. We attribute this to redundant queries introducing ambiguity during set prediction process, where each query is expected to match a unique object. These re-

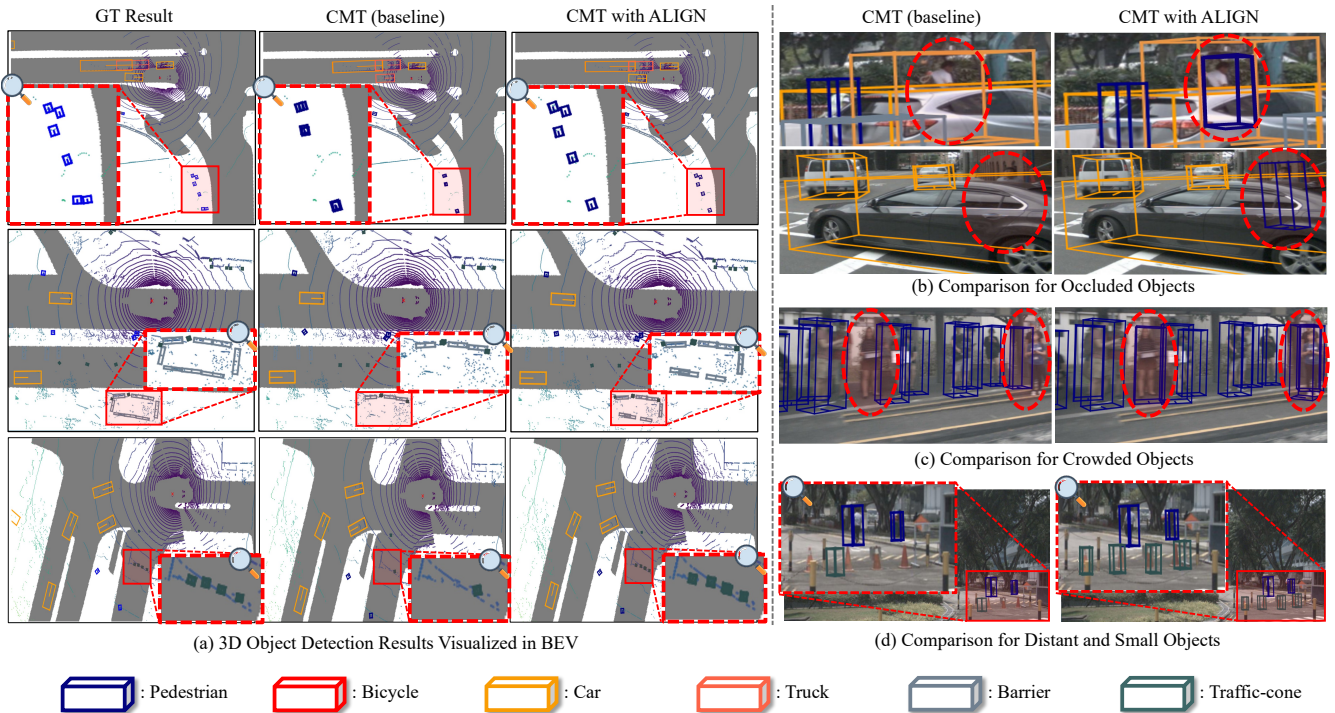


Figure 4: **Qualitative Comparison of 3D Object Detection Results with and without ALIGN.** (a) BEV visualizations show that ALIGN improves localization of small and occluded objects compared to the baseline, reducing missed detections and refining box placement. (b) Our method detects heavily occluded pedestrians missed by the baseline. (c) In crowded scenes, our method better resolves overlaps, improving object separation and robustness. (d) Detection is more accurate for distant and small instances. Red dotted regions highlight areas where ALIGN outperforms the baseline.

sults suggest that using moderate number of sampled points on objects and retaining background anchors help ensure model’s prediction reliability and broad spatial coverage.

Overall, these ablation results validate the effectiveness of each ALIGN component, with their combined use yielding consistent and complementary gains. This highlights the strength of structured, multi-stage query initialization in enhancing 3D detection performance.

Qualitative Results. In Fig. 4, we present qualitative results from the nuScenes validation set, comparing our method with the baseline. The proposed approach improves 3D object detection by addressing limitations in conventional query initialization, particularly in challenging scenarios such as occluded, distant, or crowded objects. Fig. 4(a) shows BEV visualizations, where our method reduces false negatives and improves object localization. Red-circled areas highlight regions where the baseline fails to detect objects or produces inaccurate boxes, while our method provides more reliable results. Fig. 4(b) demonstrates improved detection of occluded objects, where occlusion-aware center estimation enhances localization under severe visibility constraints. Fig. 4(c) highlights detection in crowded environments, where high object density can lead to missed detections. By dynamically balancing query distribution, our method better separates overlapping instances. Fig. 4(d) shows ALIGN’s enhanced detection on distant and small ob-

jects. By leveraging LiDAR and camera information during query initialization, ALIGN helps the model better capture geometry and context in remote areas. These results confirm that our approach effectively mitigates the weaknesses of conventional query initialization, leading to more robust and accurate scene understanding.

Conclusion

We introduce ALIGN, a structured query initialization framework that leverages LiDAR geometry and image segmentation to enhance query placement in multi-modal 3D object detection. ALIGN comprises three components—Occlusion-aware Center Estimation, Adaptive Neighbor Sampling, and Dynamic Query Balancing—that jointly guide queries toward likely object regions while maintaining background coverage. Evaluated on five representative detectors from the nuScenes benchmark, ALIGN consistently improves performance, achieving gains of up to 0.9 mAP and 1.2 NDS without altering detector architectures. Notably, it yields substantial improvements on small and occluded objects, highlighting the impact of better query initialization in challenging scenarios. As a modular and model-agnostic design, ALIGN can be easily integrated into existing detection pipelines, offering a simple yet effective enhancement for query-based 3D perception.

References

- Bai, X.; Hu, Z.; Zhu, X.; Huang, Q.; Chen, Y.; Fu, H.; and Tai, C.-L. 2022. TransFusion: Robust LiDAR-Camera Fusion for 3D Object Detection with Transformers. In *2022 IEEE/CVF Conference on Computer Vision and Pattern Recognition (CVPR)*, 1080–1089. New Orleans, LA, USA: IEEE. ISBN 978-1-66546-946-3.
- Caesar, H.; Bankiti, V.; Lang, A. H.; Vora, S.; Liong, V. E.; Xu, Q.; Krishnan, A.; Pan, Y.; Baldan, G.; and Beijbom, O. 2020. nuScenes: A Multimodal Dataset for Autonomous Driving. In *2020 IEEE/CVF Conference on Computer Vision and Pattern Recognition (CVPR)*, 11618–11628. Seattle, WA, USA: IEEE. ISBN 978-1-72817-168-5.
- Cai, Q.; Pan, Y.; Yao, T.; Ngo, C.-W.; and Mei, T. 2023. Objectfusion: Multi-modal 3d object detection with object-centric fusion. In *Proceedings of the IEEE/CVF International Conference on Computer Vision*, 18067–18076.
- Carion, N.; Massa, F.; Synnaeve, G.; Usunier, N.; Kirillov, A.; and Zagoruyko, S. 2020. End-to-end object detection with transformers. In *European conference on computer vision*, 213–229. Springer.
- Chen, X.; Zhang, T.; Wang, Y.; Wang, Y.; and Zhao, H. 2022a. FUTR3D: A Unified Sensor Fusion Framework for 3D Detection. Issue: arXiv:2203.10642 arXiv:2203.10642 [cs].
- Chen, X.; Zhang, T.; Wang, Y.; Wang, Y.; and Zhao, H. 2023a. FUTR3D: A Unified Sensor Fusion Framework for 3D Detection. In *Proceedings of the IEEE/CVF Conference on Computer Vision and Pattern Recognition (CVPR) Workshops*, 172–181.
- Chen, Y.; Yu, Z.; Chen, Y.; Lan, S.; Anandkumar, A.; Jia, J.; and Alvarez, J. M. 2023b. Focalformer3d: focusing on hard instance for 3d object detection. In *Proceedings of the IEEE/CVF International Conference on Computer Vision*, 8394–8405.
- Chen, Z.; Li, Z.; Zhang, S.; Fang, L.; Jiang, Q.; and Zhao, F. 2022b. Deformable feature aggregation for dynamic multi-modal 3D object detection. In *European conference on computer vision*, 628–644. Springer.
- Contributors, M. 2020. MMDetection3D: OpenMMLab next-generation platform for general 3D object detection. <https://github.com/open-mmlab/mmdetection3d>.
- DLPack Contributors. 2020. DLPack: Open In-Memory Tensor Structure. <https://github.com/dmlc/dlpack>.
- Drews, F.; Feng, D.; Faion, F.; Rosenbaum, L.; Ulrich, M.; and Gläser, C. 2022. DeepFusion: A Robust and Modular 3D Object Detector for Lidars, Cameras and Radars. In *2022 IEEE/RSJ International Conference on Intelligent Robots and Systems (IROS)*, 560–567.
- Gao, Z.; Wang, L.; Han, B.; and Guo, S. 2022. Adamixer: A fast-converging query-based object detector. In *Proceedings of the IEEE/CVF Conference on Computer Vision and Pattern Recognition*, 5364–5373.
- He, K.; Gkioxari, G.; Dollár, P.; and Girshick, R. 2017. Mask r-cnn. In *Proceedings of the IEEE international conference on computer vision*, 2961–2969.
- He, K.; Zhang, X.; Ren, S.; and Sun, J. 2015. Deep Residual Learning for Image Recognition. arXiv:1512.03385.
- He, L.; and Todorovic, S. 2022. Destr: Object detection with split transformer. In *Proceedings of the IEEE/CVF conference on computer vision and pattern recognition*, 9377–9386.
- Ji, H.; Liang, P.; and Cheng, E. 2024. Enhancing 3d object detection with 2d detection-guided query anchors. In *Proceedings of the IEEE/CVF Conference on Computer Vision and Pattern Recognition*, 21178–21187.
- Kuhn, H. W. 1955. The Hungarian method for the assignment problem. *Naval Research Logistics Quarterly*, 2(1-2): 83–97.
- Lee, Y.; won Hwang, J.; Lee, S.; Bae, Y.; and Park, J. 2019. An Energy and GPU-Computation Efficient Backbone Network for Real-Time Object Detection. arXiv:1904.09730.
- Li, Y.; Chen, Y.; Qi, X.; Li, Z.; Sun, J.; and Jia, J. 2022. Unifying Voxel-based Representation with Transformer for 3D Object Detection. Issue: arXiv:2206.00630 arXiv:2206.00630 [cs].
- Liang, M.; Yang, B.; Wang, S.; and Urtasun, R. 2018. Deep Continuous Fusion for Multi-sensor 3D Object Detection. In *Computer Vision – ECCV 2018*, volume 11220, 663–678. Cham: Springer International Publishing. ISBN 978-3-030-01269-4 978-3-030-01270-0.
- Liang, T.; Xie, H.; Yu, K.; Xia, Z.; Lin, Z.; Wang, Y.; Tang, T.; Wang, B.; and Tang, Z. 2022. BEVFusion: A Simple and Robust LiDAR-Camera Fusion Framework. Issue: arXiv:2205.13790 arXiv:2205.13790 [cs].
- Lin, T.-Y.; Goyal, P.; Girshick, R.; He, K.; and Dollár, P. 2017. Focal Loss for Dense Object Detection. In *Proceedings of the IEEE International Conference on Computer Vision*, 2980–2988.
- Liu, Y.; Wang, T.; Zhang, X.; and Sun, J. 2022a. PETR: Position Embedding Transformation for Multi-View 3D Object Detection. Issue: arXiv:2203.05625 arXiv:2203.05625 [cs].
- Liu, Z.; Tang, H.; Amini, A.; Yang, X.; Mao, H.; Rus, D.; and Han, S. 2022b. BEVFusion: Multi-Task Multi-Sensor Fusion with Unified Bird’s-Eye View Representation. Issue: arXiv:2205.13542 arXiv:2205.13542 [cs].
- Loshchilov, I.; and Hutter, F. 2019. Decoupled Weight Decay Regularization. arXiv:1711.05101.
- NVIDIA Corporation. 2017. NVIDIA TensorRT. <https://developer.nvidia.com/tensorrt>.
- Paszke, A.; Gross, S.; Massa, F.; Lerer, A.; Bradbury, J.; Chanan, G.; Killeen, T.; Lin, Z.; Gimelshein, N.; Antiga, L.; et al. 2019. Pytorch: An imperative style, high-performance deep learning library. *Advances in neural information processing systems*, 32.
- Raschka, S.; Patterson, J.; and Nolet, C. 2020. Machine Learning in Python: Main developments and technology trends in data science, machine learning, and artificial intelligence. *arXiv preprint arXiv:2002.04803*.
- Schubert, E.; Sander, J.; Ester, M.; Kriegel, H. P.; and Xu, X. 2017. DBSCAN revisited, revisited: why and how you

- should (still) use DBSCAN. *ACM Transactions on Database Systems (TODS)*, 42(3): 1–21.
- Smith, L. N. 2017. Cyclical Learning Rates for Training Neural Networks. Issue: arXiv:1506.01186 arXiv:1506.01186 [cs].
- Van Geerenstein, M. R.; Ruppel, F.; Dietmayer, K.; and Gavrila, D. M. 2024. Multimodal object query initialization for 3d object detection. In *2024 IEEE International Conference on Robotics and Automation (ICRA)*, 12484–12491. IEEE.
- Wang, Y.; Guizilini, V. C.; Zhang, T.; Wang, Y.; Zhao, H.; and Solomon, J. 2022a. Detr3d: 3d object detection from multi-view images via 3d-to-2d queries. In *Conference on Robot Learning*, 180–191. PMLR.
- Wang, Y.; Zhang, X.; Yang, T.; and Sun, J. 2022b. Anchor DETR: Query Design for Transformer-Based Detector. *Proceedings of the AAAI Conference on Artificial Intelligence*, 36(3): 2567–2575. Number: 3.
- Wang, Z.; Huang, Z.; Fu, J.; Wang, N.; and Liu, S. 2023. Object as Query: Lifting any 2D Object Detector to 3D Detection. arXiv:2301.02364.
- Xie, Y.; Xu, C.; Rakotosaona, M.-J.; Rim, P.; Tombari, F.; Keutzer, K.; Tomizuka, M.; and Zhan, W. 2023. Sparsefusion: Fusing multi-modal sparse representations for multi-sensor 3d object detection. In *Proceedings of the IEEE/CVF International Conference on Computer Vision*, 17591–17602.
- Yan, J.; Liu, Y.; Sun, J.; Jia, F.; Li, S.; Wang, T.; and Zhang, X. 2023a. Cross Modal Transformer: Towards Fast and Robust 3D Object Detection. arXiv:2301.01283.
- Yan, J.; Liu, Y.; Sun, J.; Jia, F.; Li, S.; Wang, T.; and Zhang, X. 2023b. Cross Modal Transformer via Coordinates Encoding for 3D Object Detection. Issue: arXiv:2301.01283 arXiv:2301.01283 [cs].
- Yan, Y.; Mao, Y.; and Li, B. 2018. SECOND: Sparsely Embedded Convolutional Detection. *Sensors*, 18(10): 3337.
- Yang, Z.; Chen, J.; Miao, Z.; Li, W.; Zhu, X.; and Zhang, L. 2022. DeepInteraction: 3D Object Detection via Modality Interaction. *Advances in Neural Information Processing Systems*, 35: 1992–2005.
- Yao, Z.; Ai, J.; Li, B.; and Zhang, C. 2021. Efficient DETR: Improving End-to-End Object Detector with Dense Prior. Issue: arXiv:2104.01318 arXiv:2104.01318 [cs].
- Zeng, Y.; Zhang, D.; Wang, C.; Miao, Z.; Liu, T.; Zhan, X.; Hao, D.; and Ma, C. 2022. LIFT: Learning 4D LiDAR Image Fusion Transformer for 3D Object Detection. In *2022 IEEE/CVF Conference on Computer Vision and Pattern Recognition (CVPR)*, 17151–17160. New Orleans, LA, USA: IEEE. ISBN 978-1-66546-946-3.
- Zhang, S.; Wang, X.; Wang, J.; Pang, J.; Lyu, C.; Zhang, W.; Luo, P.; and Chen, K. 2023. Dense distinct query for end-to-end object detection. In *Proceedings of the IEEE/CVF conference on computer vision and pattern recognition*, 7329–7338.
- Zhao, Y.; Lv, W.; Xu, S.; Wei, J.; Wang, G.; Dang, Q.; Liu, Y.; and Chen, J. 2024. Detsr beat yolos on real-time object detection. In *Proceedings of the IEEE/CVF Conference on Computer Vision and Pattern Recognition*, 16965–16974.
- Zhou, Z.; Zhao, X.; Wang, Y.; Wang, P.; and Foroosh, H. 2022. CenterFormer: Center-Based Transformer for 3D Object Detection. *Computer Vision – ECCV 2022*, 13698: 496–513.
- Zhu, B.; Jiang, Z.; Zhou, X.; Li, Z.; and Yu, G. 2019. Class-balanced Grouping and Sampling for Point Cloud 3D Object Detection. Issue: arXiv:1908.09492 arXiv:1908.09492 [cs].
- Zhu, X.; Su, W.; Lu, L.; Li, B.; Wang, X.; and Dai, J. 2021. Deformable DETR: Deformable Transformers for End-to-End Object Detection. In *International Conference on Learning Representations (ICLR)*.

Supplementary Material

More Implementation and Evaluation Details

Class-Specific Depth Offset in OCE

In Occlusion-aware Center Estimation (OCE) module, object centers are estimated by projecting LiDAR points onto the image plane and computing a representative surface point p_{surf} from image-guided segmentation. As LiDAR captures only visible surfaces, p_{surf} typically lies near the front surface, introducing a systematic depth bias.

To correct this, we apply a class-specific depth offset d along the LiDAR ray to approximate the true center. Motivated by (Ji, Liang, and Cheng 2024), which leverages class-wise size priors to improve localization, we assign compensation offsets per class for accurate object center estimation. Larger objects receive greater offsets, while smaller or symmetric ones require minimal adjustment.

Table 7 summarizes the class-wise bounding box statistics from (Ji, Liang, and Cheng 2024) and our derived depth offset ranges. Each row lists the min/max values for object width (w_{\min}, w_{\max}), height (h_{\min}, h_{\max}), length (l_{\min}, l_{\max}), and depth offset range (d_{\min}, d_{\max}). These structured priors are integrated into our OCE module, improving box orientation and scale. As shown in Table 8, class-specific offsets generally help reduce Average Scale Error (ASE) and Average Orientation Error (AOE), supporting their role in refining box geometry.

Category	(w_{\min}, w_{\max})	(h_{\min}, h_{\max})	(l_{\min}, l_{\max})	(d_{\min}, d_{\max})
Car	(1.4, 2.8)	(1.2, 3.1)	(3.4, 6.6)	(0.6, 3.9)
Pedestrian	(0.3, 1.0)	(1.0, 2.2)	(0.3, 1.3)	(0.2, 1.4)
Bus	(2.6, 3.5)	(2.8, 4.6)	(6.9, 13.8)	(1.3, 7.5)
Truck	(1.7, 3.5)	(1.7, 4.5)	(4.5, 14.0)	(0.8, 7.6)
Trailer	(2.2, 2.3)	(3.3, 3.9)	(1.7, 14.0)	(0.8, 7.4)
Constr. veh.	(2.1, 3.4)	(2.0, 3.0)	(3.7, 7.6)	(1.0, 4.4)
Motorcycle	(0.4, 1.5)	(1.1, 2.0)	(1.2, 2.8)	(0.2, 1.9)
Bicycle	(0.4, 0.9)	(0.9, 2.0)	(1.3, 2.0)	(0.2, 1.5)
Traffic cone	(0.2, 1.2)	(0.5, 1.4)	(1.3, 2.0)	(0.1, 1.4)
Barrier	(1.7, 3.6)	(0.8, 1.4)	(0.3, 0.8)	(0.2, 2.0)

Table 7: Per-class bounding box size ranges and corresponding depth offset ranges used in OCE. Each prior is computed from dataset-level statistics and helps compensate for depth bias by guiding more accurate center localization. All values are in meters.

Details of LiDAR Clustering in ANS

In the Adaptive Neighbor Sampling module, object candidates are extracted by applying DBSCAN (Schubert et al. 2017) to LiDAR points filtered within a predefined region-of-interest (ROI). The neighborhood radius ϵ is set to 0.6, and the minimum number of points to form a cluster is 7.

To accelerate clustering, we utilize the GPU-based DBSCAN implementation from NVIDIA’s cuML library (Raschka, Patterson, and Nolet 2020), achieving over $50\times$ speedup compared to the CPU version. As the LiDAR

data is represented as PyTorch (Paszke et al. 2019) tensors on the GPU, we convert it to the format required by cuML using DLpack (DLpack Contributors 2020)-based zero-copy transformation. Although the clustering step introduces some additional latency, our implementation minimizes its impact, enabling ANS to operate efficiently without compromising inference speed.

Occlusion-Aware Benchmarking on nuScenes

To assess detection robustness under occlusion, we adopt the nuScenes visibility annotations, which assign each object a level from 1 (heavily occluded) to 4 (fully visible) based on the visible ratio of its 2D bounding box: Level 1 corresponds to 0–40%, Level 2 to 40–60%, Level 3 to 60–80%, and Level 4 to 80–100% visibility.

While prior work has considered object distance, visibility-specific evaluation has been overlooked. We present the first detailed analysis of occlusion-level detection on a large-scale urban dataset. This exposing performance drops under heavy occlusion hidden in conventional metrics and emphasizing the importance of robust detection for partially visible objects in urban driving.

All evaluations are conducted on the nuScenes validation set (6019 samples), with each visibility level evaluated independently using only matching ground truths and predictions to isolate occlusion effects. As shown in Table 2 of the main paper, performance degrades as visibility decreases. With Level 1 (heavily occluded) alone comprising 19.2% of all objects, this highlights the importance of occlusion-aware detection for reliable autonomous driving. To support future research, we will release the occlusion-level evaluation code for nuScenes upon publication.

Ablation-wise Computational Cost

We evaluate the computational overhead of each ALIGN module on the nuScenes validation set using a single NVIDIA A6000 GPU. All experiments are based on the CMT (Yan et al. 2023b) detector. Table 10 reports the average inference latency per sample and GPU memory usage.

Among the modules, OCE introduces the highest computational overhead, adding 198 ms of latency and 2408 MB of memory usage compared to the baseline, as reported in Table 10 (b). This can be mitigated by applying quantization (e.g., TensorRT (NVIDIA Corporation 2017)) or limiting segmentation to key views like the front camera, reducing computation proportionally.

In contrast, ANS introduces minimal overhead, adding 36 ms latency and 272 MB memory usage, as observed in configuration (c), demonstrating high computational efficiency. This is enabled by GPU-accelerated DBSCAN via cuML for fast clustering of LiDAR points. Memory overhead stays low by avoiding full LiDAR loading; instead, DLpack copies only ROI-filtered points already in memory, reducing redundant transfers and memory use.

When OCE and ANS are jointly applied, the total overhead reaches 239 ms latency and 2887 MB memory, as seen

Method	Metric	Car	Truck	Bus	Tra.	Const.	Ped.	Moto.	Bike	Cone	Bar.	Total
CMT	ASE(\downarrow)	14.0	17.8	16.8	21.8	44.8	27.6	23.1	25.7	31.5	27.1	25.0
CMT + ALIGN		14.0	17.9	16.7	21.7	44.5	27.5	22.3	25.1	30.9	27.1	24.7 <small>(-0.3)</small>
CMT	AOE(\downarrow)	4.00	4.20	4.00	35.9	83.6	28.5	22.0	30.2	–	4.30	24.1
CMT + ALIGN		3.80	3.80	4.00	33.8	79.8	26.9	20.1	27.2	–	4.10	22.6 <small>(-1.5)</small>

Table 8: Class-specific depth offsets improve ASE and AOE on the nuScenes validation set.

Visibility Level	Number of Ground-Truth Objects
Level 1 (0–40%)	23,437 (19.2%)
Level 2 (40–60%)	12,779 (10.5%)
Level 3 (60–80%)	17,815 (14.6%)
Level 4 (80–100%)	67,830 (55.7%)
Total	121,861

Table 9: Distribution of ground-truth objects by visibility level in the nuScenes validation set (6019 samples).

in (d). Adding DQB in (e) does not increase cost further, as it only redistributes the existing queries without introducing additional heavy computation or extra feature extraction.

Overall, ALIGN introduces a manageable amount of computational overhead, and each module is independently optimizable. More importantly, it enhances occlusion-robust detection without modifying the original detector architecture, making it a practical, plug-and-play solution for safety-critical perception systems.

	OCE	ANS	DQB	Lat. (ms)	Mem. (MB)
(a)				297	6959
(b)	✓			495 <small>(+198)</small>	9367 <small>(+2408)</small>
(c)		✓		333 <small>(+36)</small>	7231 <small>(+272)</small>
(d)	✓	✓		536 <small>(+239)</small>	9846 <small>(+2887)</small>
(e)	✓	✓	✓	536 <small>(+239)</small>	9846 <small>(+2887)</small>

Table 10: Ablation-wise latency and memory usage on nuScenes validation set.

More Visualization Results

Figure 5 compares detection results across the ground truth, baseline, and CMT with ALIGN on scenes containing heavy occlusion and crowded objects. While nearby objects such as vehicles and bicycles are detected similarly across models, ALIGN significantly improves localization of partially occluded or distant instances, such as barriers and pedestrians. In the highlighted region, CMT alone misses or mislocalizes several occluded objects, whereas ALIGN accurately recovers occluded pedestrians and yields more precise bounding boxes for barriers.

However, heavily occluded and distant objects such as traffic-cones, which are small and thin, remain challenging

to detect even with OCE and ANS, as they often lack sufficient visual and geometric cues for reliable localization, indicating room for further improvement.

Figure 6 presents additional qualitative results on occluded and crowded scenes. In (a), ALIGN accurately detects pedestrians and rear vehicles heavily occluded by nearby objects, demonstrating the effectiveness of OCE and ANS in recovering missing instances. In (b), performance in crowded settings is boosted by semantically guided query initialization via OCE, which places queries near object-consistent regions. Furthermore, ANS and DQB compensate for incomplete segmentation in crowded scenes. ANS supplements detection by placing additional queries anchors around clustered LiDAR points. DQB further reallocates query budget toward regions where object boundaries are unclear or multiple objects overlap, helping capture targets that are partially hidden behind others.

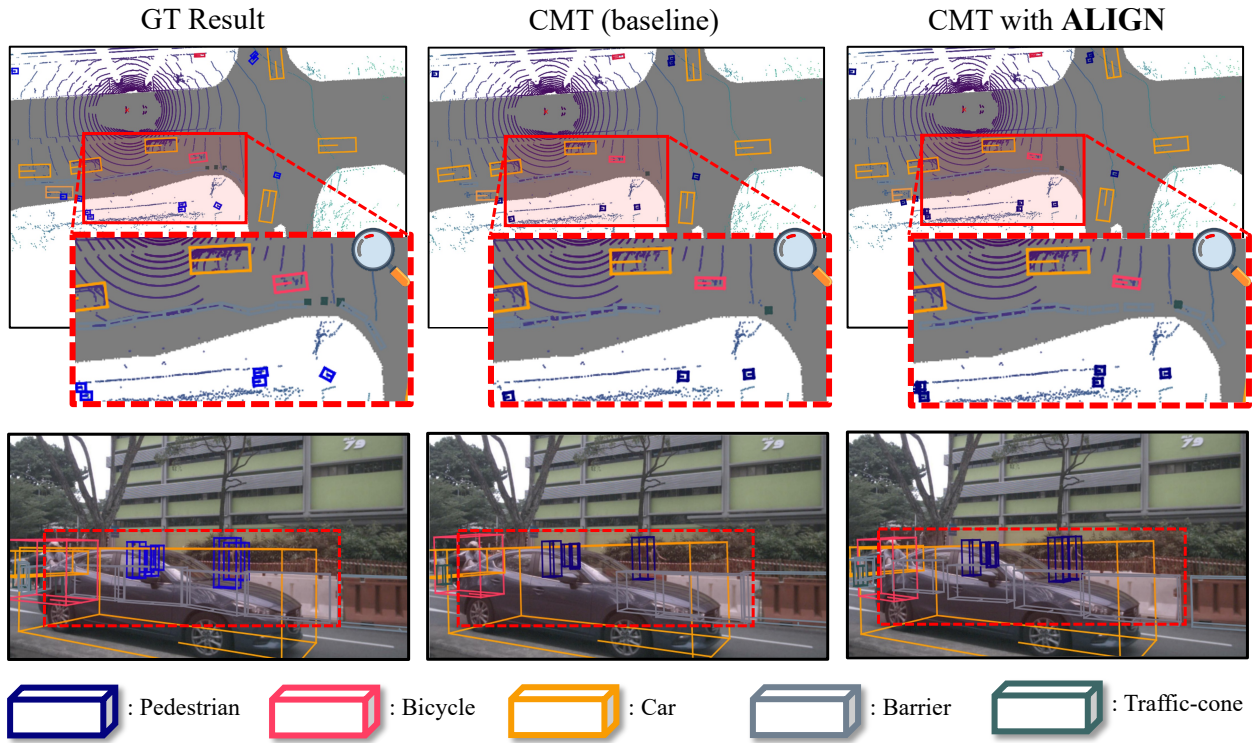


Figure 5: **Qualitative comparison across GT, baseline, and CMT with ALIGN.** ALIGN improves detection of occluded and crowded objects (red dotted regions), localizing barriers and occluded pedestrians missed by the baseline. All models struggle with small, heavily occluded traffic cones, indicating room for further improvement.

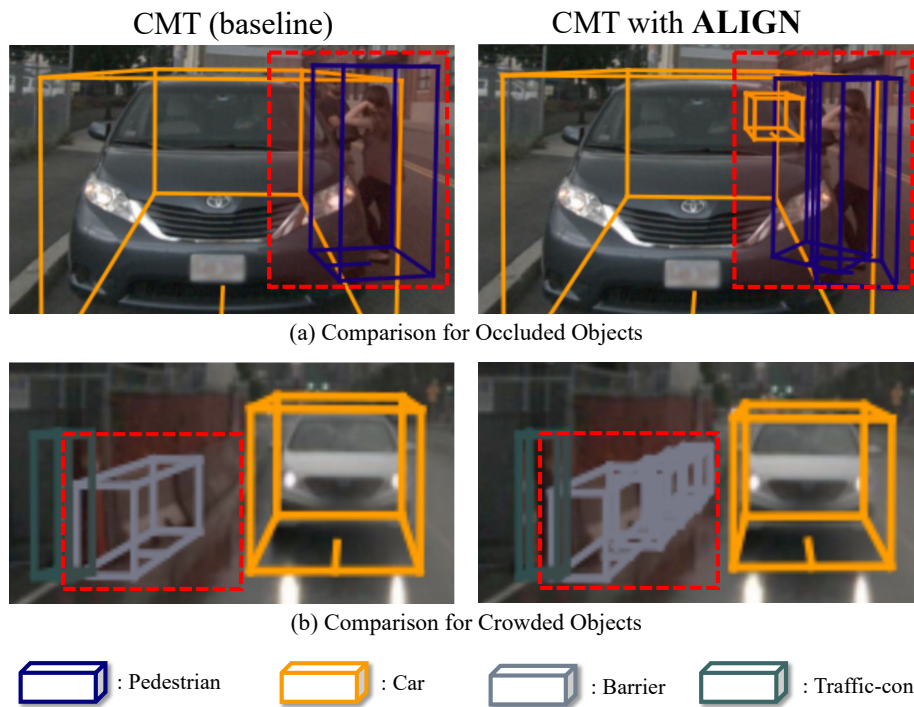


Figure 6: **Additional qualitative results on occluded and crowded scenes.** In (a), ALIGN recovers pedestrians and vehicles heavily occluded by other objects. In (b), it improves detection in crowded scenes by guiding queries to object-relevant areas and adaptively handling ambiguous regions.